

Calibrating Large-area Mask Projection Stereolithography for Its Accuracy and Resolution Improvements

Chi Zhou, Yong Chen*

Epstein Department of Industrial and Systems Engineering
University of Southern California, Los Angeles, CA 90089

*Corresponding author: yongchen@usc.edu, (213) 740-7829

ABSTRACT Reviewed, accepted September 15, 2009

Solid freeform fabrication (SFF) processes based on mask image projection such as digital micro-mirror devices (DMD) have the potential to be fast and inexpensive. More and more research and commercial systems have been developed based on such digital devices. However, a digital light processing (DLP) projector based on DMD has limited resolution and certain image blurring. In order to use a DLP projector in the large-area mask projection stereolithography, it is critical to plan mask images in order to achieve high accuracy and resolution. Based on our previous work on optimized pixel blending, we present a calibration method for capturing the non-uniformity of a projection image by a low cost off-the-shelf DLP projector. Our method is based on two calibration systems, a geometric calibration system that can calibrate the position, shape, size, and orientation of a pixel and an energy calibration system that can calibrate the light intensity of a pixel. Based on both results, the light intensity at various grayscale levels can be approximated for each pixel. Developing a library of such approximation functions is critical for the optimized pixel blending to generate a better mask image plan. Experimental results verify our calibration results.

1. INTRODUCTION

Current market trends such as consumer demand for variety, shorter product life cycles, and higher product quality have resulted in the need for more efficient and robust manufacturing paradigm. Solid freeform fabrication (SFF) can fabricate parts directly from computer-aided design (CAD) models without part-specific tooling and fixtures. Thus it can significantly shorten product development cycle while satisfying customized design requirements.

1.1. SFF Processes based on DMD

The large-area mask projection stereolithography is a SFF process based on mask image projection on a big surface area (e.g. 250x250mm). In this process, the 3-Dimensional (3D) CAD model of an object is firstly sliced by a set of horizontal planes. Each slice is then converted into a 2-Dimensional (2D) image which serves as a mask corresponding to the layer to be built. The mask image is then projected by a light projection device onto a surface to form the layer of the object. By repeating the process, 3D objects can be formed on a layer-by-layer basis. This process can form a whole layer of multiple objects simultaneously and dynamically. Therefore, it provides a potentially faster approach that is independent from part size and geometry. It also removes the requirement of an accurate XY motion control subsystem. Therefore the process can be relatively inexpensive.

Several research systems have been developed before based on the mask image projection process [1-12]. Both digital micromirror devices (DMD) and light crystal display (LCD) have been used as light projection device, and visible-light-cured photopolymer or UV curable resin have been used as the raw material. These research systems mainly focus on fabricating micro parts (hence mask projection micro stereolithography). In addition, commercial systems based on DMD have also been developed such as the *Perfactory* system from *Envisiontec GmbH* [13] and the *V-Flash* system from *3D Systems Inc.* [14].

1.2. Pixel Blending for DMD-based SFF Processes

The mask image used in a mask image projection system is one of the most important process parameters. A well planned mask image is especially important for the large-area mask projection stereolithography. Since a big platform area is required while the resolution of a DMD device is limited by the number of pixels (e.g. 1024x768), the pixel size of a projected image will increase accordingly. Therefore, the achievable accuracy and resolution will decrease in the built models.

To address such a problem, an optimization pixel blending method [15] has been proposed. The method is based on the observations that: (1) the light beam of a pixel will spread to its neighboring pixels; (2) the light intensity of a pixel more follows *Gaussian* distribution; (3) the light intensity at any position is actually the sum of the light intensities contributed by all the neighboring pixels (defined as *pixel blending*); (4) a desired energy input can be achieved by intelligently manipulating the grayscale values of each pixel; (5) such exposure energy will then lead to a cured layer with desired shape. We mathematically formulate the pixel blending problem in an optimization model, and use optimization tools to solve the problem. Both simulation and physical experiments have been carried out to validate the effectiveness and efficiency of the optimized pixel blending method. Figure 1 shows an example of dimensional accuracy study. Notice the traditional method will lose the small portion while the pixel blending method can get the shape quite close to the original one. Figure 2 shows the case of surface quality study. It is obvious that the building result based on the optimized pixel blending method has a much better surface quality.

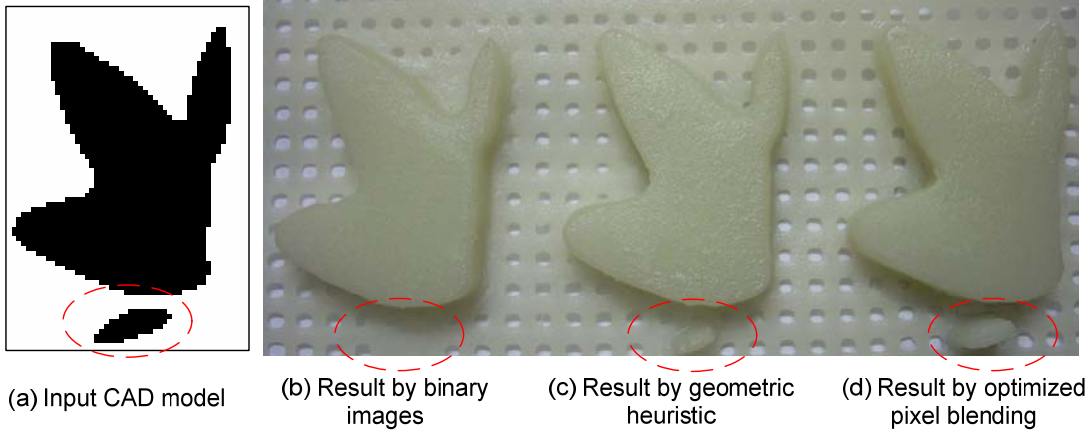


Figure 1. A simple test case for dimensional accuracy study [15].

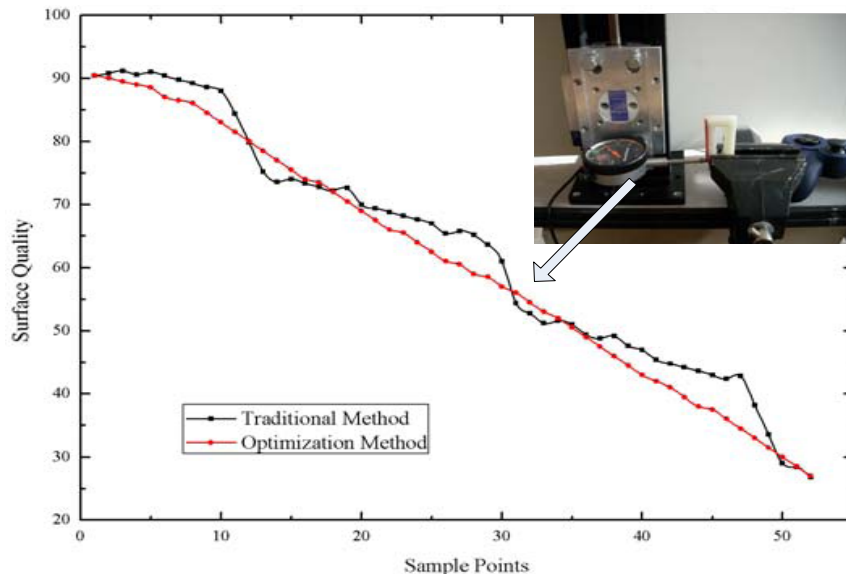


Figure 2. A simple test case for surface quality study [15].

1.3. Projection Image Calibration for Optimized Pixel Blending

As demonstrated in our previous work, the pixel blending of light intensity would give us tremendous capability in selectively solidifying resin into a desired shape. However, in the pixel blending method presented in [15], we used one *Gaussian* function (at the center of the image) to approximate the light intensity of all pixels. This may not be suitable for a low cost off-the-shelf DLP projector. Due to the low cost optic components used in such a projector, the projection image may have distortion and the light intensity is non-uniform. These geometric and energy differences would affect our pixel blending results. In this paper, we present a method to calibrate such non-uniformity of a projection image. By incorporating the calibration results in our mask image planning framework, the part quality for the large-area mask projection stereolithography will be significantly improved.

2. PROJECTION IMAGE CALIBRATION PRINCIPLE

In our large-area mask projection stereolithography system, we used an off-the-shelf DLP projector (*CASIO XJ-S36*) with 1024x768 pixels. The pixel size is around 0.265 mm when a platform is set at 271x204 mm. Considering its small size, it is rather difficult to use light measurement devices to directly measure the properties of a pixel. In this paper, we propose a novel calibration method based on dividing the pixel properties into two categories:

- (1) Relative properties: For a pixel's geometric properties such as its position, shape, size, and orientation, it is more important to measure the relative light intensity. That is, we can manipulate the incident light beam at our wish. As long as the measured light intensity after the manipulation is proportional to the incident light intensity, the measurement of such relative properties will be accurate.
- (2) Absolute properties: For a pixel's energy properties such as its light intensity, no manipulation will be allowed. We have to measure the incident light beam directly.

Accordingly, we develop two types of calibration systems: geometric and energy calibration systems. Different measurement methods have been developed in the systems. Finally the light distribution of a pixel can be characterized by combining the geometric and energy calibration results.

(1) Geometric Calibration Principle:

We tried the method of mounting a camera directly toward the projected light beam of a DLP projector. However, the geometric properties of a pixel are hard to be measured from the captured images since it is difficult to remove the highlight at the surface of the lenses. To overcome the drawback, we develop a method based on measuring the light transmission from a translucent medium. That is, we add some translucent medium at the focus plane of a projected image. Hence, the incident light beam (K_i) is decomposed into three portions: reflection (K_r), absorption (K_a) and transmission (K_t). In addition, $K_i \propto K_r$; $K_i \propto K_a$; $K_i \propto K_t$; and $K_i = K_r + K_a + K_t$. From these optical equations, we can calibrate either portion of light intensity to compute the geometric properties of a pixel since they are proportional to K_i .

We tested the method of measuring K_r . That is, the light shoots on the medium and a picture is taken by using the light reflected from the medium. However, in this method, a camera can not be mounted overhead the image; otherwise, it would block the light. The angle between the lens and the projection plane would result in large distortion in the picture. Extra efforts are required to correct such distortions.

Instead, in the proposed method based on measuring K_t , a camera can be directly mounted under the medium so no distortion exists in the pictures taken by the camera. The light transmitted from the medium (K_t) can be measured directly. We use a digital microscope device (x50) to take a magnified picture for each pixel. The images can then be analyzed since the light intensity is approximately proportional to the grayscale level of the image. Accordingly the geometric properties of each pixel can be calibrated.

(2) Energy Calibration Principle:

We use a photosensor and RC circuit to directly measure the light intensity of incident light. Since a photosensor has limited sensitivity and relatively big size ($>3\text{ mm}$), we can only measure the light intensity of a small region (e.g. 20×20 pixels). Hence the light intensity of a pixel is computed by averaging the measuring result of the region that the pixel belongs to. Our method is based on the assumption that the light intensity changes only slightly within a small region (e.g. $2 \times 2\text{ mm}$) while it may vary greatly from regions to regions. Based on our experimental results and the optical error analysis [16], we believe such an assumption is valid.

By combining the geometric and energy calibration results, the light distribution of each pixel can be characterized. An illustration of the whole calibration system is shown in Figure 3.

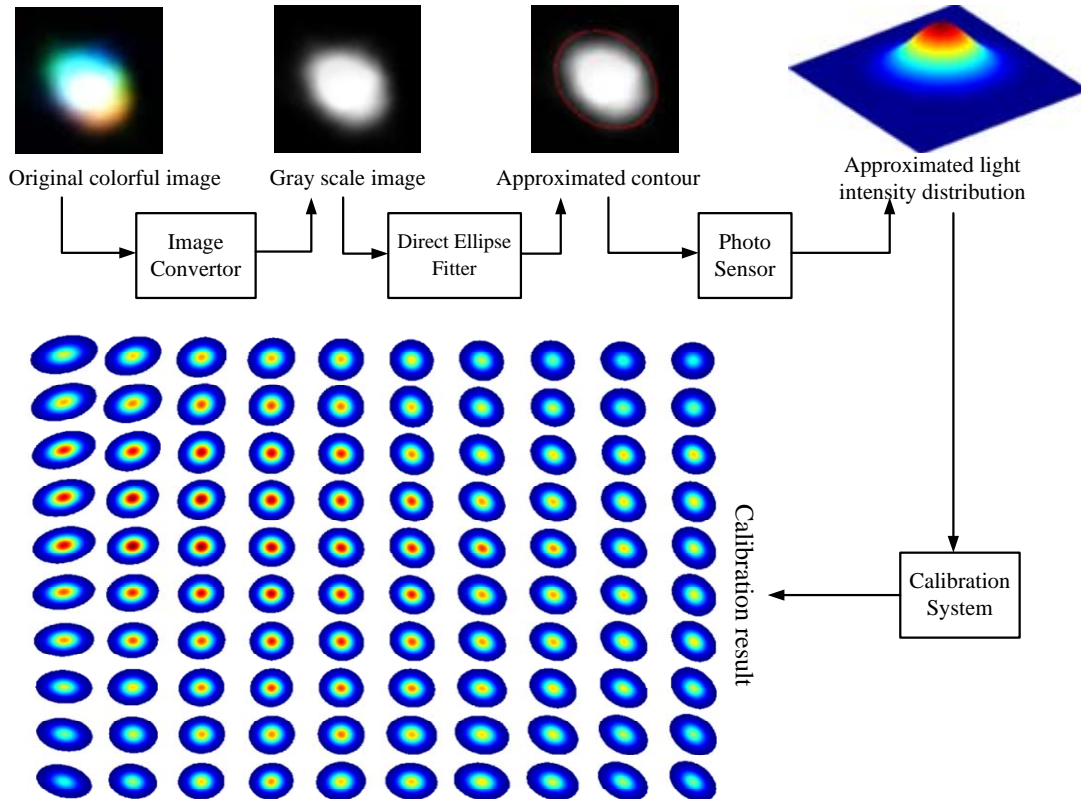


Figure 3. Pixel calibration framework for a DLP projector.

The remainder of the paper is organized as follows. In section 3, we present the geometric calibration system. In section 4, we describe the energy calibration system. The calibration results based on the presented systems are discussed in section 5. In section 6, we present the experimental results for verifying our result. Finally, we draw conclusion and discuss future work in section 7.

3. GEOMETRIC CALIBRATION SYSTEM

3.1. Calibration Setup

The setup of our geometric calibration system is shown in Figure 4. We use ProScope HR [17] with a 50 times lens to capture the image of a pixel. A high resolution XY linear stage is used to transform the microscope to cover the whole area of a platform. As mentioned before, some medium (paper, plastic, etc) is added between the microscope and the projector to avoid the highlight. The

microscope is then placed directly under the medium such that the focus plane of the microscope is coplanar to the projection image.

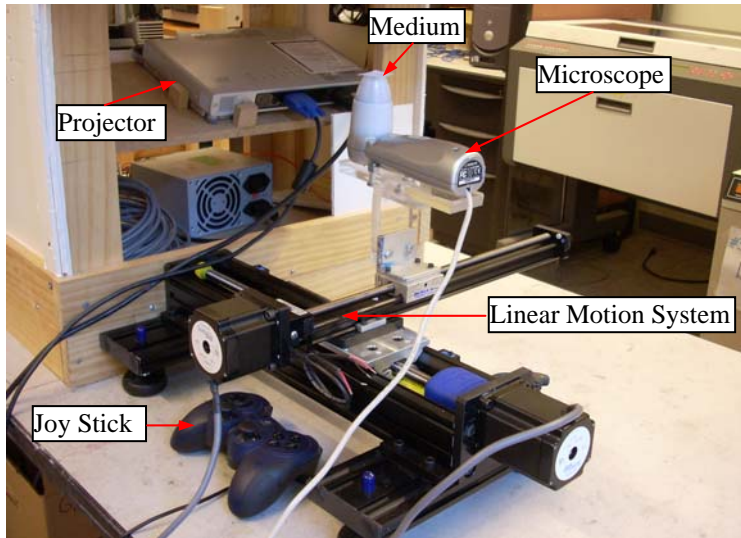


Figure 4. Setup of our geometric calibration system.

As shown in Figure 5, we developed a software system to integrate the linear motion of the microscope and its functions such as picture taking and saving. The client window can dynamically show the captured pictures. Initially the microscope is set at the original position of the projection image. At each position, we control the projector to turn on a related pixel and control the microscope to take a picture. Then image analysis algorithms are run in parallel to compute the geometric parameters. After that, the motion control system will translate the microscope to a new pixel position. The procedure is repeated until all the pixels are measured and analyzed.

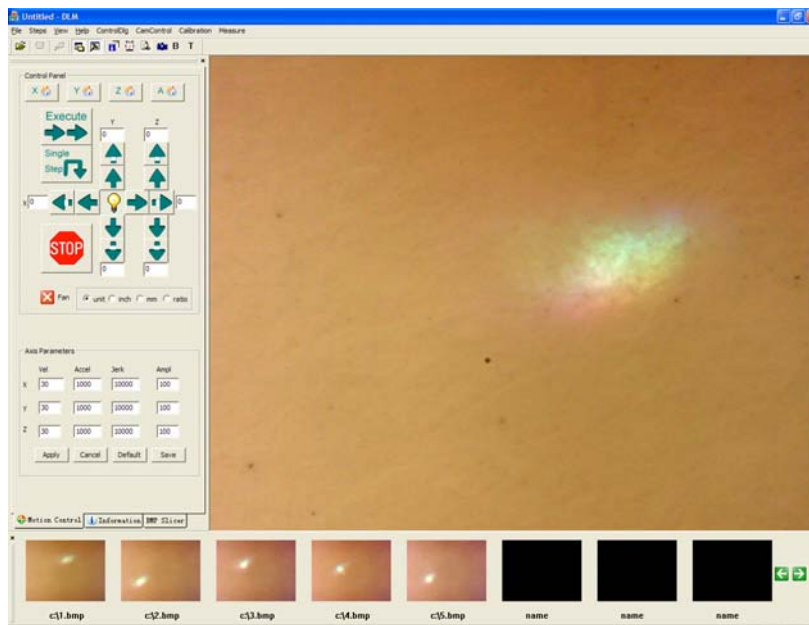


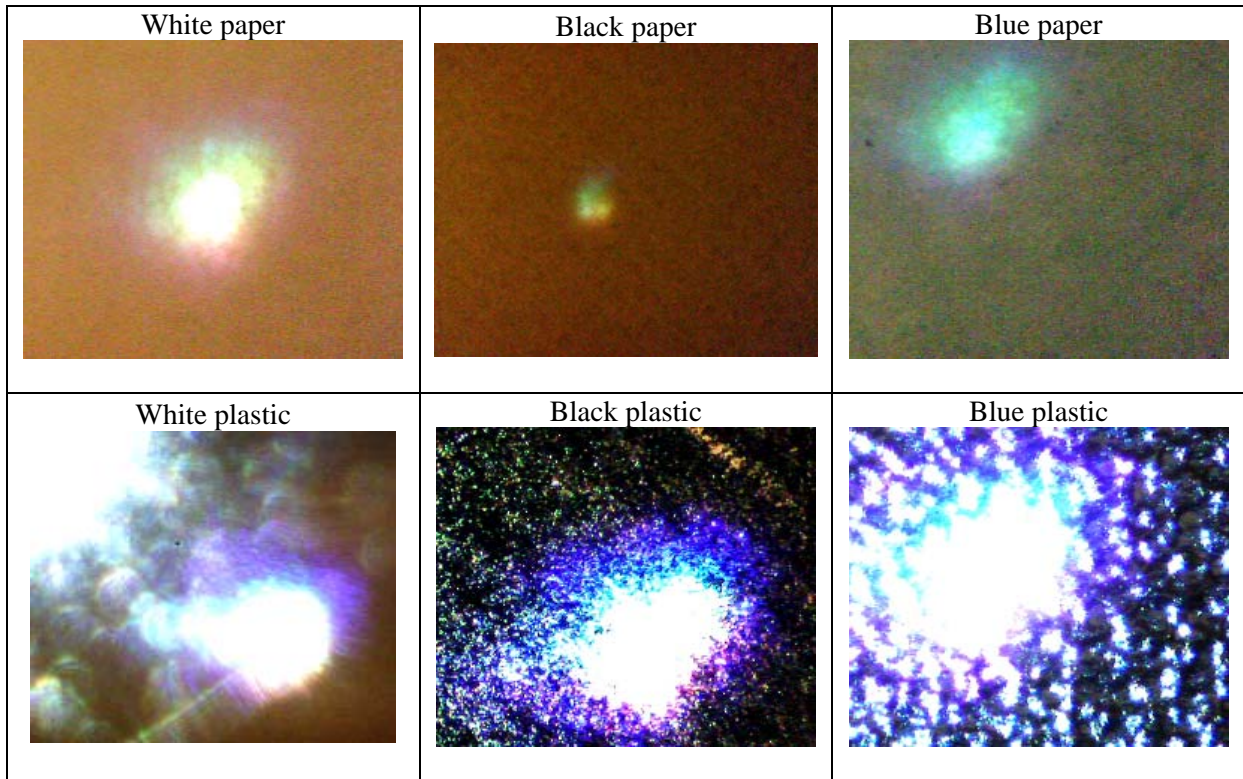
Figure 5. Motion control and image analysis interface.

3.2. Medium Selection

As discussed in section 2, some media should be added for measuring light transmission. Thus, a related issue is to choose a proper medium to achieve the best measuring quality. Different kinds of

medium have been tried for a good balance between reflection (K_r), absorption (K_a) and transmission (K_t). After multiple tests, we select a white paper as the medium in our system. The white paper can give us good picture quality such as high contrast, good penetration, and low noise. Some other test results are also shown in Table 1. The black paper and blue paper absorbed too much light and the plastics reflect too much light. Thus they are not good candidates for measuring K_r . Other translucent media is still possible; however, opaque or transparent ones are not appropriate.

Table 1: Pictures under different mediums.



3.3. Image Analysis

The pixel grayscale values in a digital image carry the intensity information. The grayscale value of a pixel varies from black (at the lowest intensity) to white (at the highest intensity). The pictures take by the microscope are represented in RGB colors (i.e. Red, Green, and Blue). To convert a color picture into a grayscale image, we can calculate the effective brightness or luminance of a RGB value. Based on it, we can then compute a grayscale value to match the brightness. The approach we used is based on a commonly used conversion equation:

$$grayscale = 0.299*r+0.587*g+0.114*b,$$

where r , g , b is the red, green and blue components of the color image.

As shown in the picture of “white paper” in Table 1, the environmental light has effects on the grayscale value of a pixel. That is, the background of the paper has the brown grain textures due to the environmental light. Our method to remove such effects is to take two pictures for each pixel exposure. That is, when moving the microscope to a position, we take a picture of the pixel exposure; after turning off the pixel, we then take another picture without the pixel exposure. The subtraction between the two pictures turns out to be the picture of the pure pixel exposure. To reduce the noise, we may also take the two pictures for multiple times and use the average of all the subtraction picture as the final result. The above process is illustrated in Table 2. An alternative way is to take pictures in a dark

room to physically avoid the effect of the environmental light. Some test results are shown in Table 3.a. The results are better than those based on the previous method.

Table 2: Grayscale conversion and picture subtraction.

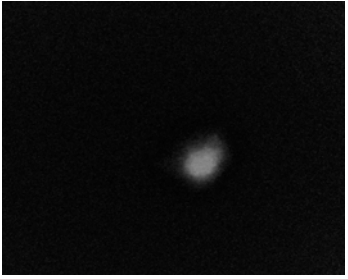
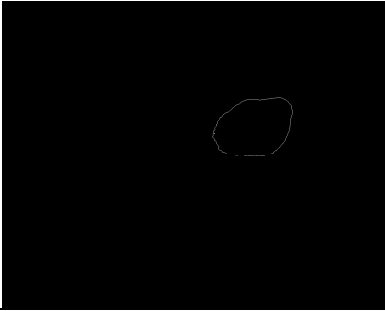
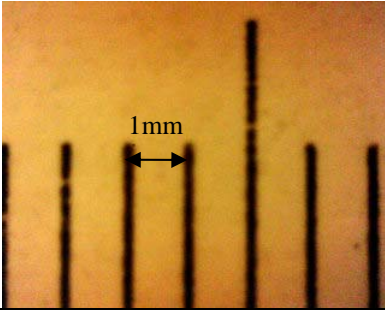
	A Pixel Exposure	Background	Subtraction between “A Pixel Exposure” and “Background”
Colorful picture			
Grayscale Picture			

Table 3: Grayscale conversion and picture subtraction.

(a) Original colorful picture 	(b) Grayscale picture after low-pass filter 	(c) Above threshold 
(d) Boundary 	(e) Fitted ellipses 	(f) Ruler under microscope (in the same scale) 

To further remove the noise, we can also apply the low-pass filter to the grayscale image. The smoothed picture is shown in Table 3.b. We set a threshold 0.1 (the grayscale value is normalized between 0 and 1) as the cut-off value. We then use a recursive algorithm to get the effective light region and the corresponding boundary which is shown in Table 3.c-d. Based on the assumption of *Gaussian* distribution, the contour for a *Gaussian* function is an ellipse. We use a fast non-iterative ellipse fit method, direct ellipse fit [18], to approximate the pixel shape. The parameters can then be computed (refer to Appendix A for the detail procedure). An example of the approximated ellipse is shown in Table 3.e. For a reference of the actual size, we also show an image of a ruler in Table 3.f. As shown in the figures, the real size of a pixel is about 1 mm, which is about 3~4 times of the ideal pixel size. This result validated the fact that the light beam spreads to the neighborhood pixels.

3.4. Geometric Calibration of the Whole Platform

We apply the previous method to all the pixels in a projection image related to the platform. In our setup, the projection image has a resolution of 1024x768. Hence the above process needs to be run automatically in order to calculate the shape, size, orientation and position of each individual pixel. However, due to the intrinsic distortion, we found the project plane can not be adjusted into a perfect rectangle. The best one we use in our system is shown in Figure 6. Since our microscope has a limited image size (around 6 mm). We need to compensate the distortion in the motion control in order to capture the exposure of all the pixels.

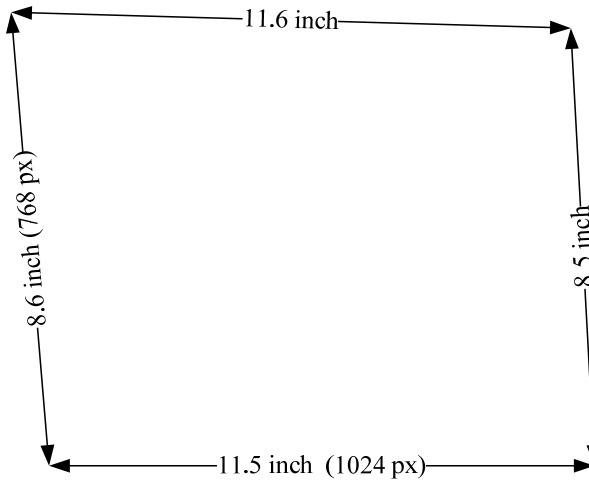


Figure 6. Dimension and shape of the image.

4. ENERGY CALIBRATION SYSTEM

The geometric calibration system can capture the size, shape, orientation and position of a pixel. However, it is hard to know the ratio between reflection (K_r), absorption (K_a) and transmission (K_t) in the incident light beam (K_i). Hence, we use light measurement sensors to directly measure the light intensity of an incident light beam. A photoresistor can exhibit a resistance change in proportional to the exposed light intensity. Hence it can serve our purpose. An important consideration for selecting a photoresistor is the linearity of the output signal. An output that is linearly proportional to the input intensity (illumination) is highly desirable. We selected a photoresistor (350-00009 by *Parallax* [19]). According to its technical specifications, the following equation shows the relationship between the resistance of a photoresistor and the illumination E :

$$R = AE^{-\alpha},$$

where R is the resistance of the device, A and α (sensitivity) are constants dependent on manufacturing process and material type. The photoresistor we used is made from type ϕ material and its

$\alpha = 0.8$. Based on the equation, we can easily compute the light intensity by measuring the photoresistor's resistance.

The setup of our energy calibration system is shown in Figure 7. We use a microcontroller from *Parallax* [19] to integrate the measurement results of the resistance into the whole automated calibration system. We construct a simple RC circuit and use a *RCTIME* function provided by the microcontroller to measure the resistance of the photoresistor. To reduce the effect of fluctuation, we measured the resistance 100 times and take the average in computing the light intensity of each pixel.

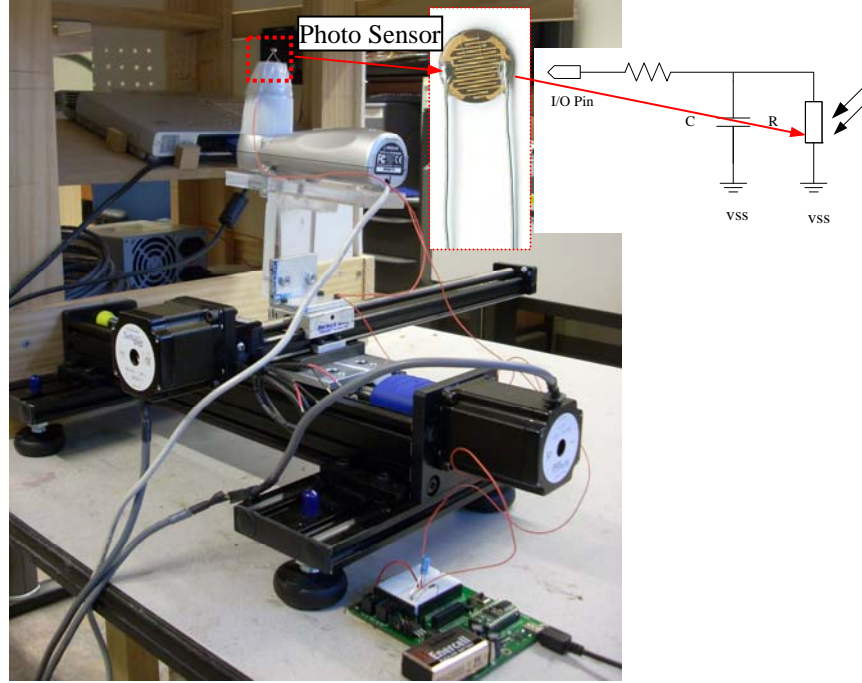


Figure 7. Setup of our energy calibration system.

The measured light intensity of a pixel can then be used in computing the height A of its *Gaussian* function. That is, suppose the *Gaussian* function is:

$$g(x, y) = A \exp \left\{ -\frac{1}{2} \left[\frac{(x - x_0)^2}{\sigma_x^2} + \frac{(y - y_0)^2}{\sigma_y^2} \right] \right\},$$

where (x_0, y_0) is the center point of the pixel, σ_x and σ_y are used to characterize the shape of the pixel. We can read the values of $x_0, y_0, 3\sigma_x, 3\sigma_y$ from the previous geometric calibration system. Note that we do not consider the orientation of the pixel, since the orthogonal system would simplify the calculation without affecting the problem. $\tilde{x}_s = [x_0, y_0]$, $\tilde{l} = [3\sigma_x, 3\sigma_y]$.

Hence the light intensity can be calculated as follows:

$$\begin{aligned} I &= \iint g(x, y) dx dy = \int_{-3\sigma_x+x_0}^{3\sigma_x+x_0} \int_{-3\sigma_y+y_0}^{3\sigma_y+y_0} A \exp \left\{ -\frac{1}{2} \left[\frac{(x - x_0)^2}{\sigma_x^2} + \frac{(y - y_0)^2}{\sigma_y^2} \right] \right\} dx dy \\ &= A \int_{-3\sigma_x+x_0}^{3\sigma_x+x_0} \int_{-3\sigma_y+y_0}^{3\sigma_y+y_0} \frac{1}{2\pi\sigma_x\sigma_y} \exp \left\{ -\frac{1}{2} \left[\frac{(x - x_0)^2}{\sigma_x^2} + \frac{(y - y_0)^2}{\sigma_y^2} \right] \right\} dx dy \approx A \int_{-3\sigma_x+x_0}^{3\sigma_x+x_0} \int_{-3\sigma_y+y_0}^{3\sigma_y+y_0} \frac{1}{2\pi\sigma_x\sigma_y} dx dy \end{aligned}$$

Thus, we have the relationship: $A \propto \frac{I}{\sigma_x\sigma_y} \propto \frac{R^{-\frac{1}{\alpha}}}{\sigma_x\sigma_y} \propto \frac{RCTIME^{-\frac{1}{\alpha}}}{\sigma_x\sigma_y}$.

5. CALIBRATION RESULTS

The calibration results based on the aforementioned calibration systems are presented as follows.

5.1. Geometric Calibration Results

Our initial experimental results showed that a pixel has a similar distortion with the ones in its immediate neighborhood. Hence, instead of measuring each pixel which will take quite a long time, we can only sample a portion of the pixels that are uniformly distributed. The properties of other pixels can then be interpolated from the calibrated pixels.

We present the geometric calibration result of $10 \times 10 = 100$ sampled pixels for a grayscale value of 255 (full light intensity) as shown in Figure 8. For the sake of observation convenience, the size of the ellipses is magnified 300 times. The center point and orientation of each ellipse represent the center point and the orientation of the sampled pixel. We also perform the same experiments for lower light intensities. The results for the projection images with grayscale=200 and grayscale=150 are shown in Figure 9 and Figure 10 respectively.

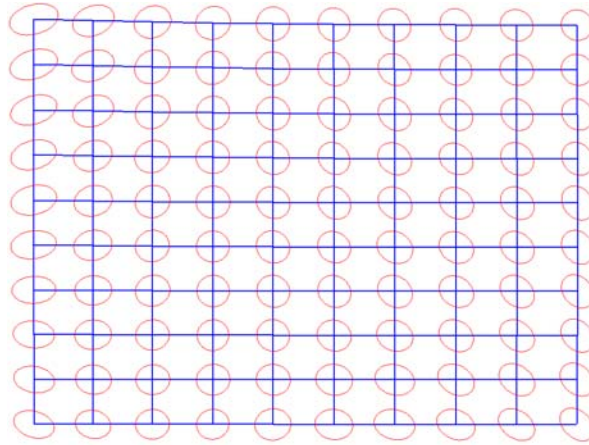


Figure 8. Distribution of 1 pixel (grayscale=255).

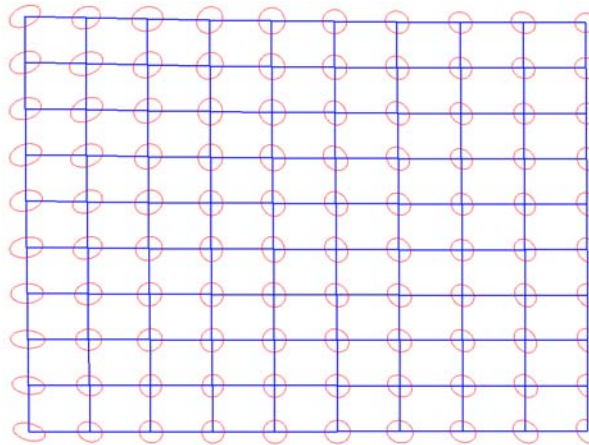


Figure 9. Distribution of 1 pixel (grayscale=200).

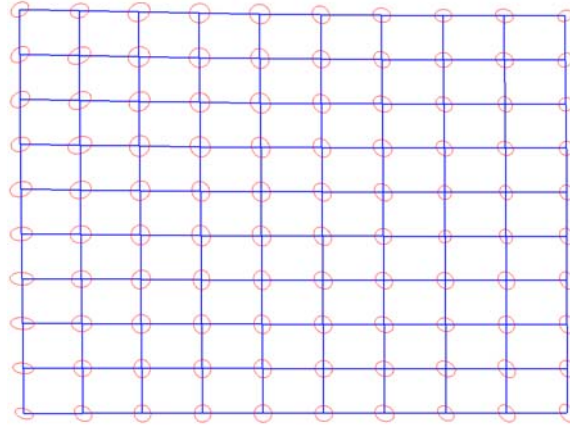


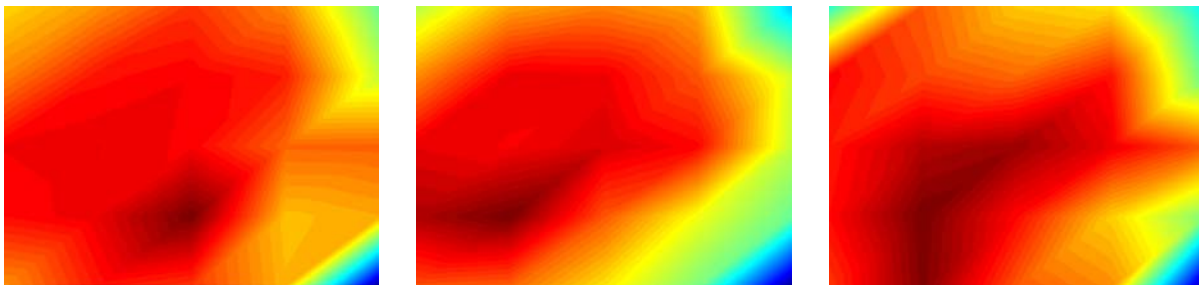
Figure 10. Distribution of 1 pixel (grayscale=150).

Based on the results, we can draw the following conclusions and observation:

- (1) The pixels are non-uniformly distributed in the screen;
- (2) The distribution is consistent for different grayscale levels;
- (3) The shapes and orientations of the pixels are change gradually and smoothly in both vertical and horizontal directions, thus we can interpolate the properties of a pixel base on the calibrated ones in its neighbors;
- (4) The center portion has less distortion. Thus using center portion of the image to build part can achieve better quality;
- (5) Pixel grid has distortion. The pixels are not located in the same line in both vertical and horizontal directions and the whole screen is not a perfect rectangle.
- (6) The pixels are not evenly distributed in the projection image (with some shifting).

5.2. Energy Calibration Results

From the readout of the photosensor, we can compute the light intensities according to the resistor-intensity equation. A visualization of an experimental result on the pixels' light intensity is shown in Figure 11. In the figure, different colors are used to represent the light intensity values. The light intensity is higher if the related pixel has a redder color; and the light intensity is lower if the pixel has a bluer color.



(a) grayscale=255

(b) grayscale=200

(c) grayscale=150

Figure 11. Light intensity distributions for different grayscale levels.

Based on the results, we can draw the following conclusions:

- (1) The energy is non-uniformly distributed in the projection image;
- (2) The center of the image has higher light intensity;
- (3) The energy distribution is consistent for different grayscale levels.

5.3. Approximation Functions of Pixels

By integrating the geometric and energy calibration results, we can compute an approximation function for the light intensity of each calibrated pixel by using the following equation:

$$g(x, y) = A \exp \left\{ -\frac{1}{2} \left[\left(\frac{(x - x_0) \cos(\theta) - (y - y_0) \sin(\theta)}{\sigma_x} \right)^2 + \left(\frac{(x - x_0) \sin(\theta) + (y - y_0) \cos(\theta)}{\sigma_y} \right)^2 \right] \right\}$$

We can specify x_0 , y_0 , σ_x , σ_y and θ from the geometric calibration system. Combined with the energy calibration result, we can compute the parameter A . The computed approximation functions for different grayscale levels are shown in Figure 12 to Figure 14.

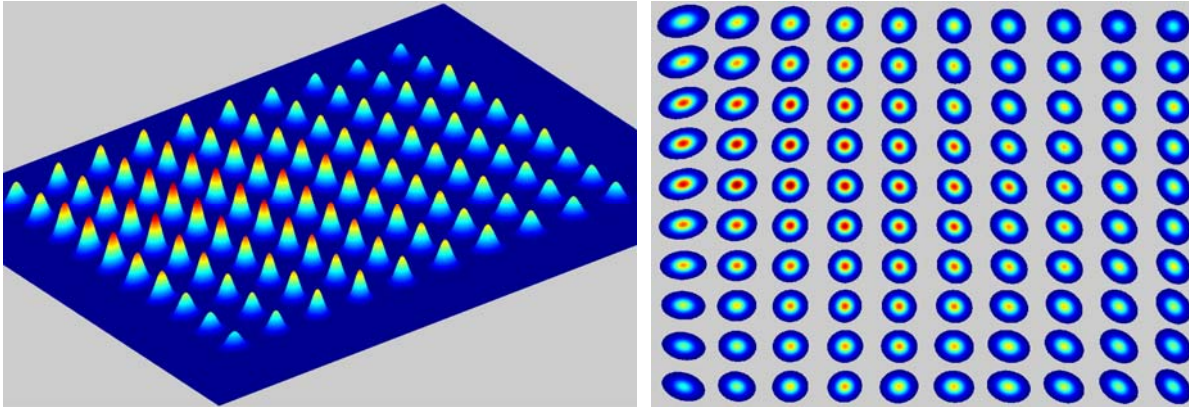


Figure 12. Pixel calibration (grayscale=255).

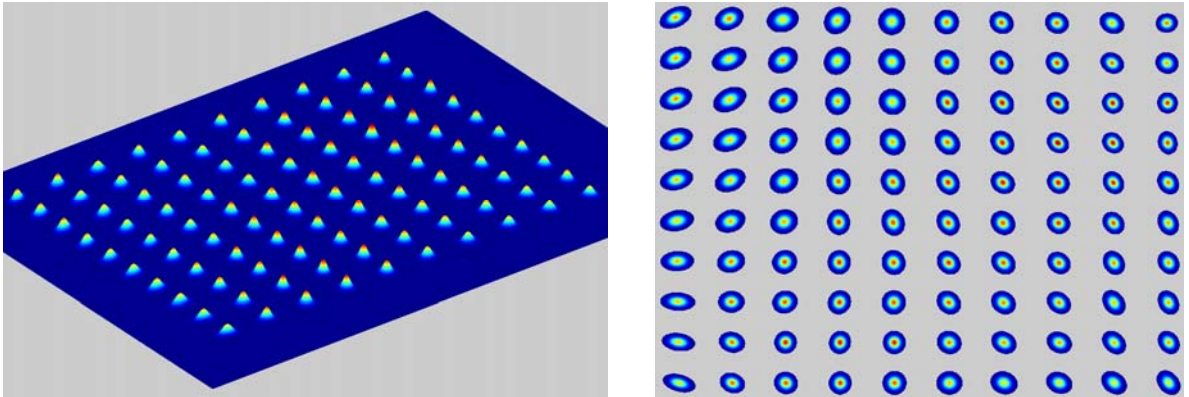


Figure 13. Pixel calibration (grayscale=200).

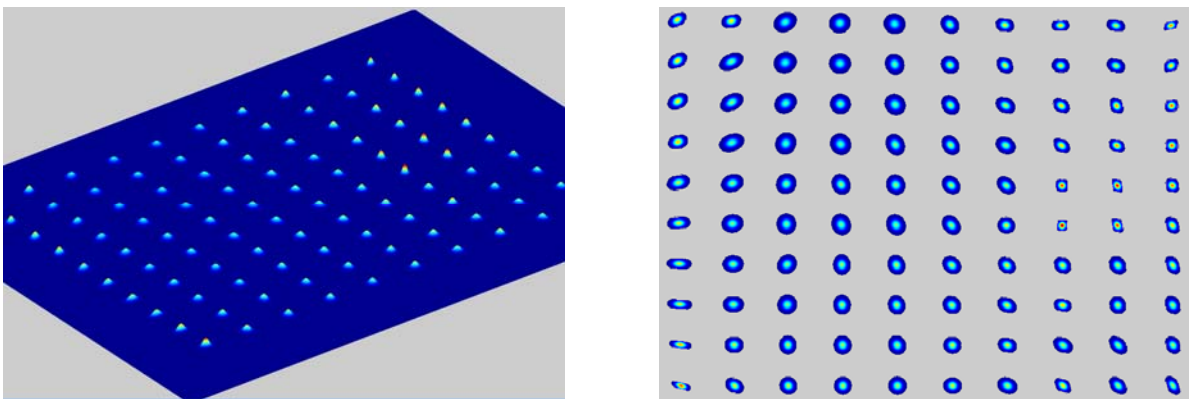


Figure 14. Pixel calibration (grayscale=150).

6. VERIFICATION OF CALIBRATION RESULTS

6.1 Shape Verification

To verify the idea of pixel blending as discussed in Section 1.2 (i.e. the convolution of light intensity of neighboring pixels), we investigate 2x2 pixels for the full grayscale case (i.e. grayscale=255). We sample 5x5 different positions; for each position, we repeat the procedure as presented in the geometric calibration. The measured distribution results are shown in Figure 15.(a). We then compute the convolution of the 2x2 pixels based on the calibration result of a single pixel. The simulated result are shown in Figure 15.(b). A comparison of the two figures illustrates that the measured and simulated shapes are close. Hence it verifies the pixel blending idea.

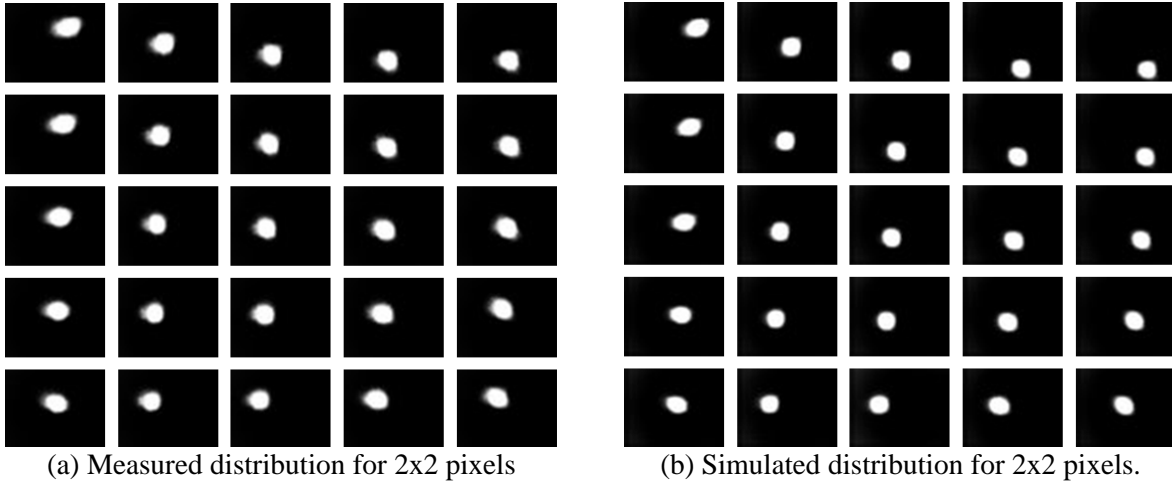


Figure 15. Pixel blending verification.

We also investigate 2x2 pixels for lower grayscale cases to show the consistence of the distribution. The results are given in Figure 16. As can be seen from the figures, the shape and the orientation are consistent with the single pixel case (refer to Figure 9 and Figure 10). Only the sizes are increased.

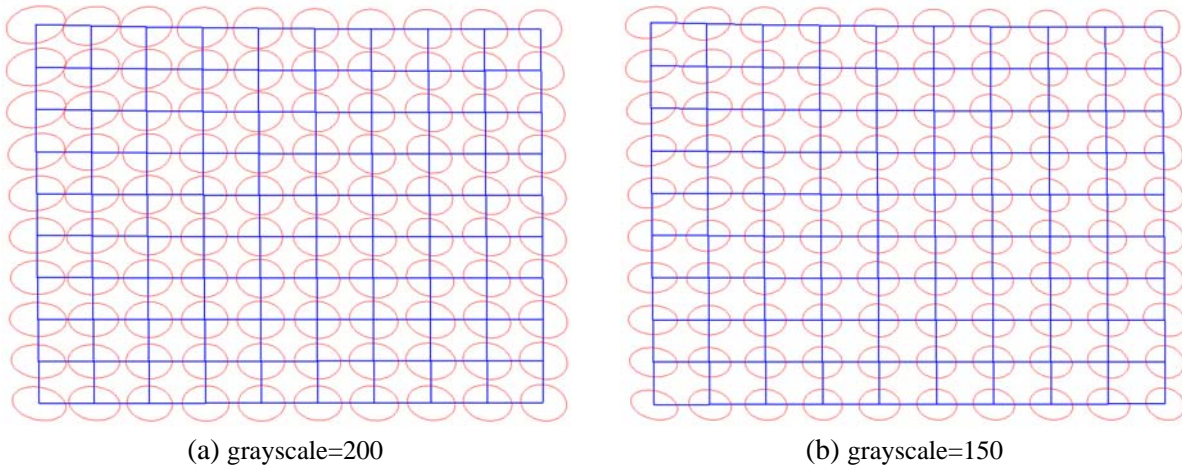


Figure 16. Distributions of 2x2 pixels.

We further performed physical experiments to verify the calibrated shapes. We spread a thin layer of resin on a red plastic plate, and then turn on 8x8 pixels at the left top corner and the left bottom corner respectively. The resin is solidified after several minutes. We clean up the liquid resin,

mark the cured part with blue color, and then put them under a microscope. The magnified pictures are shown in Figure 17. Based on the figures, we can clearly see the different orientations at different places. Further, the orientations are consistent with our calibration result as shown in Figure 8.

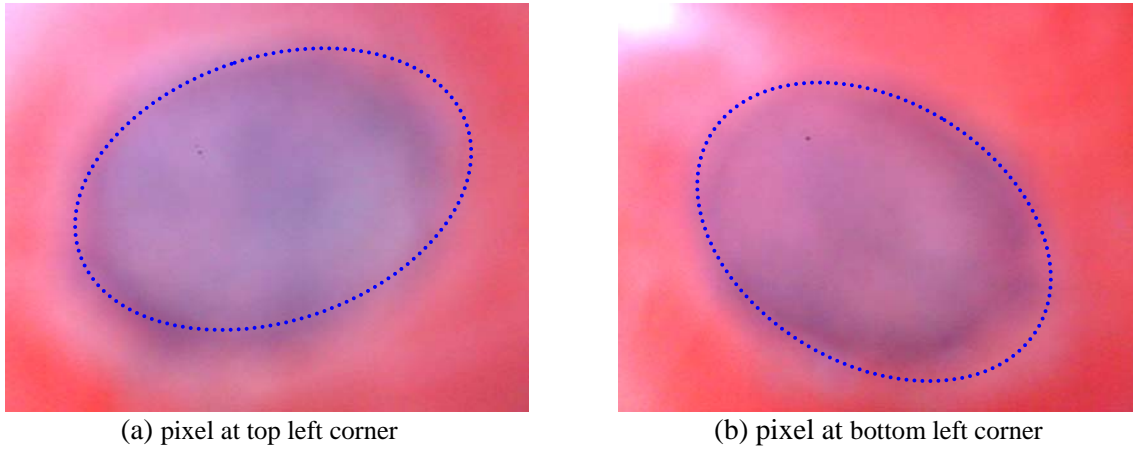


Figure 17. Physical experiment results for shape verification.

6.2. Energy verification

Similar physical experiment has been performed to verify the calibration result of the energy distribution. We turned on 4x4 pixels at the center and near the boundary (middle-right). We then expose them for the same period of time. The result is shown in Figure 18. It is obvious that the sizes of the cured shapes are different. Thus the input energy levels are different. The light intensity at the center is stronger since the related cured shape is bigger.

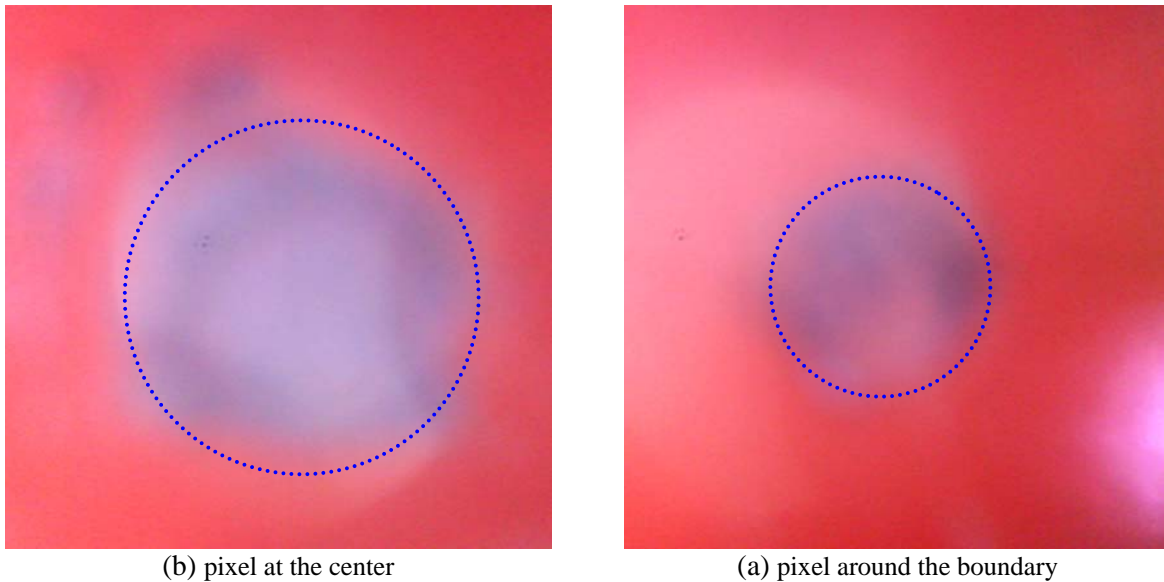


Figure 18. Physical experiment result for energy verification.

7. CONCLUSION AND FUTURE WORK

Mask image planning is an important process planning step for the large-area mask projection stereolithography. Optimized pixel blending is a mask image planning technique that can significantly increase the accuracy and resolution of the SFF process. To further improve its accuracy and resolution, we present a light intensity calibration system to capture the non-uniformity of a low cost off-the-shelf DLP projector. The calibration of the important pixel properties is conducted in two steps, geometric

and energy calibrations. In the geometric calibration, magnified pictures are taken and the geometric parameters of a pixel are computed based on image analysis. In the energy calibration, the light intensity was indirectly calculated by using a photosensor. Finally the integrated calibration results enable us to compute a library of light intensity functions. Such approximation functions for each pixel can correctly simulate the pixel blending results.

Our future work includes the following. (1) We will incorporate the calibration results in our optimized pixel blending system. This will require us to improve our optimization solver to consider such approximation functions for each pixel. (2) We would like to investigate the large-area mask projection stereolithography based on multiple DLP projectors for better part quality.

REFERENCES

1. Bertsch, A., J. Jezequel, and J. Andre (1997). *Study of Spatial Resolution of a new 3D Microfabrication Process: the Microstereolithography Using a Dynamic Mask-generator Technique*. Journal of Photochemistry and Photobiology, A: Chemistry, Vol. 107, No. 1-3.
2. Chatwin C., M. Farsari, S. Huang, M. Heywood, P. Birch, R. Young, J. Richardson (1998), *UV Microstereolithography System that Uses Spatial Light Modulator Technology*, Applied Optics, Vol. 37, pp.7514-22.
3. Farsari M., S. Huang, P. Birch, F. Claret-Tournier, R. Young, D. Budgett, C. Bradfield, C. Chatwin (1999), *Microfabrication by Use of Spatial Light Modulator in the Ultraviolet: Experimental Results*, Optics Letters, Vol. 24, No. 8, pp. 549-50.
4. Monneret S., V. Loubere, and S. Corbel (1999), *Microstereolithography Using Dynamic Mask Generator and a Non-coherent Visible Light Source*, Proc. SPIE, Vol.3680, pp.553-561.
5. Luo, Ren; J. Tzou; and W. Lee (2000). *The Development of LCD Panel Display Based Rapid Prototyping System for Advanced Manufacturing*. Proceedings of IEEE International Conference on Robotics & Automation. San Francisco, CA.
6. Bertsch A., P. Bernhard, C. Vogt, P. Renaud (2000), *Rapid Prototyping of Small Size Objects*, Rapid Prototyping Journal, Vol. 6, Number 4, pp. 259-266.
7. Hadipoespito, G., Y. Yang, H. Choi, G. Ning, X. Li (2003). *Digital Micromirror Device based Microstereolithography for Micro Structures of Transparent Photopolymer and Nanocomposites*. Proceedings of the Solid Freeform Fabrication Symposium, Austin Texas, pp. 13-24.
8. Stampfl, J.; H. Fouad; S. Seidler; R. Liska; F. Schwager; A. Woesz; and P. Fratzl (2004). *Fabrication and Moulding of Cellular Materials by Rapid Prototyping*. Int. J. Materials and Product Technology, Vol. 21, No. 4, pp 285-296.
9. Sun C., N. Fang, D. Wu, X. Zhang (2005). *Projection Micro-Stereolithography Using Digital Micro-mirror Dynamic Mask*. Sensors and Actuators A. Vol. 121, pp. 113-120.
10. Cheng, Y., M. Li, J. Lin, J. Lai, C. Ke, and Y. Huang (2005). *Development of Dynamic Mask Photolithography*. Proceedings of IEEE International Conference on Mechatronics. Taipei, Taiwan.
11. Y. Lu, G. Mapili, G. Suhali, S.C. Chen, K. Roy (2006). *A Digital Micro-mirror Device (DMD)-based System for the Microfabrication of Complex, Spatially Patterned Tissue Engineering Scaffolds*, Journal of Biomedical Materials Research A, Vol. 77A (2), pp. 396-405.
12. Limaye, A. S. and D. W. Rosen (2007), *Process planning for Mask Projection Stereolithography*. Rapid Prototyping Journal, Vol. 13, No. 2, pp. 76-84.
13. EnvisionTEC: <http://www.envisiontec.de>.
14. V-Flash desktop modeler: <http://www.modelin3d.com>.
15. Zhou, C., Y. Chen, and R. A. Waltz. *Optimized Mask Image Projection for Solid Freeform Fabrication*. Proceedings of ASME Internal Design Engineering Technical Conferences. August 30-September 2, 2009, San Diego, California, USA

16. Limaye, A.S. (2004). *Design and Analysis of a Mask Projection Micro-Stereolithography System*. Master Thesis, Georgia Institute of Technology, Atlanta, GA.
17. <http://www.bodelin.com/proscopehr/>
18. A. W. Fitzgibbon, M. Pilu, R. B. Fisher. *Direct Least Squares Fitting of Ellipses*. IEEE Trans. PAMI, Vol. 21, pages 476-480 (1999).
19. <http://www.parallax.com/>

APPENDIX A: COMPUTING ELLIPSE PARAMETERS

The output of the direct ellipse fit is in the form of $ax_1^2 + bx_1x_2 + cx_2^2 + dx_1 + ex_2 + f = 0$, where $\| [a, b, c, d, e, f] \| = 1$. From this equation, we can not get the size, orientation and center point of the ellipse. Denote the axis size as \tilde{l} , the center point as \tilde{x}_s , the angle as θ .

Define the following notations: $\tilde{B} = \begin{pmatrix} a & \frac{b}{2} \\ \frac{b}{2} & c \end{pmatrix}$, $\tilde{b} = \begin{pmatrix} d \\ e \end{pmatrix}$, $\tilde{b}_0 = f$, the equation can be rewritten as:

$\tilde{x}'\tilde{B}\tilde{x} + \tilde{x}'\tilde{b} + \tilde{b}_0 = 0$. Thus, the center point is the stationary point $\tilde{x}_s = -\frac{1}{2}\tilde{B}^{-1}\tilde{b}$.

Denote $\tilde{z} = \tilde{x} + \tilde{x}_s$ and substitute \tilde{x} by \tilde{z} , the original equation can be further rewritten as $(\tilde{z} + \frac{1}{2}\tilde{B}^{-1}\tilde{b})'\tilde{B}(\tilde{z} + \frac{1}{2}\tilde{B}^{-1}\tilde{b}) + (\tilde{z} + \frac{1}{2}\tilde{B}^{-1}\tilde{b})'\tilde{b} + \tilde{b}_0 = 0$. The simplified equation is: $\tilde{z}'\tilde{B}\tilde{z} - \frac{1}{4}\tilde{b}'\tilde{B}^{-1}\tilde{b} + \tilde{b}_0 = 0$,

which can be further written as $\frac{\tilde{z}'\tilde{B}\tilde{z}}{\frac{1}{4}\tilde{b}'\tilde{B}^{-1}\tilde{b} - \tilde{b}_0} = 1$. Denote the eigenvalue of matrix $\left(\frac{\tilde{B}}{\frac{1}{4}\tilde{b}'\tilde{B}^{-1}\tilde{b} - \tilde{b}_0} \right)$ as \tilde{e} ,

we can get the axis size as $\tilde{l} = \sqrt{1/\tilde{e}}$.

The angle θ can be calculated as $\theta = \begin{cases} \frac{b}{a-c} & a \neq c \\ \frac{\pi}{4} & a = c \end{cases}$

Based on the above parameters, we can reversely get the parametric equation of the ellipse:

$$\tilde{x}_t = \left(\tilde{l}_{x_1} \cos(t), \tilde{l}_{x_2} \sin(t) \right)', \quad t \in [0, 2\pi) \quad \text{and} \quad \tilde{x} = \begin{pmatrix} \tilde{x}_{t_1} & \tilde{x}_{t_2} \end{pmatrix} \begin{pmatrix} \cos(\theta) & \sin(\theta) \\ -\sin(\theta) & \cos(\theta) \end{pmatrix} + \tilde{x}_s$$